Experiments in Fluids 7, 412–420 (1989)

Experiments in Fluids

The shadowgraph method in convection experiments

S. Rasenat, G. Hartung, B. L. Winkler and **I. Rehberg**

Physikalisches Institut der Universität Bayreuth, D-8580 Bayreuth, F. R. Germany

Abstract. The shadowgraph method is applied to thermal convection experiments and electro-hydrodynamic convection (EHC) in nematic liquid crystals. In both cases convection leads to a spatially periodic field of the refractive index causing a spatially periodic intensity modulation of parallel light passing the cell. Close to the onset of convection the temperature or director field is given by linear stability analysis. Knowing these functions the determination of their amplitudes becomes possible by means of the shadowgraph method. The method is demostrated using various examples of thermal and EHC convection experiments.

1 Introduction

Homogeneous systems driven from equilibrium can develop a spatial structure when a threshold value of an external forcing parameter is exceeded. A popular example in fluid dynamics is the Rayleigh-Bénard convection – fluid heated from below and cooled from above gives rise to a convective flow when the temperature difference exceeds a critical value (for reviews see Busse 1978, 1980). A less known example is the onset of convection in a nematic liquid crystal when the fluid is embedded between two parallel electrodes. If the AC-Voltage applied to the electrodes exceeds a critical value, convection sets in the form of parallel rolls – the so called Williams domains (for reviews, see Goossens 1978; Blinov 1983). Both systems are often used for experimental work dealing with spatio-temporal complexity and chaos presumably because of their simplicity – in both cases no mechanically moving parts are needed to drive the flow and the external control parameter (temperature difference or voltage) can be adjusted with a resolution of more than 10^{-3} of the critical value. The most popular measuring technique to explore the convection patterns seems to be the shadowgraph method (Ahlers et al. 1985; Heutmaker et al. 1985; Steinberg et al. 1986; Kolodner et al. 1986 for examples in thermal convection) (Joets and Ribotta 1986; Lowe et al. 1986 for examples in EHC). This popularity stems from simplicity: all that is needed is parallel light and a camera. The sensitivity of the method, however, allows the observation of the onset of convection even in gases (Pocheau et al. 1985).

The principle of the method used in this paper is shown in Fig. 1. Parallel light is sent through the convection pattern, and the image of the convection pattern is obtained by a camera or photodiodes positioned at some distance from the cell. With the experimental setup shown in Fig. 1 only quasi one-dimensional patterns as those in rectangular boxes or narrow convection channels (Rehberg et al. 1987) can be observed. In order to make two-dimensional patterns visible, the light is sent vertically through the cell. The sensitivity of the shadowgraph method permits a visualization of the flow pattern close to the critical point for the onset of convection. Here we concern ourselves with measurements in the neighbourhood of this point. In Sect. 2 we will calculate the thermal convection paths for light passing through the cell and the light intensity at several distances from the cell. In Sect. 3 the same is done for electrohydrodynamic convection in liquid crystal layers.

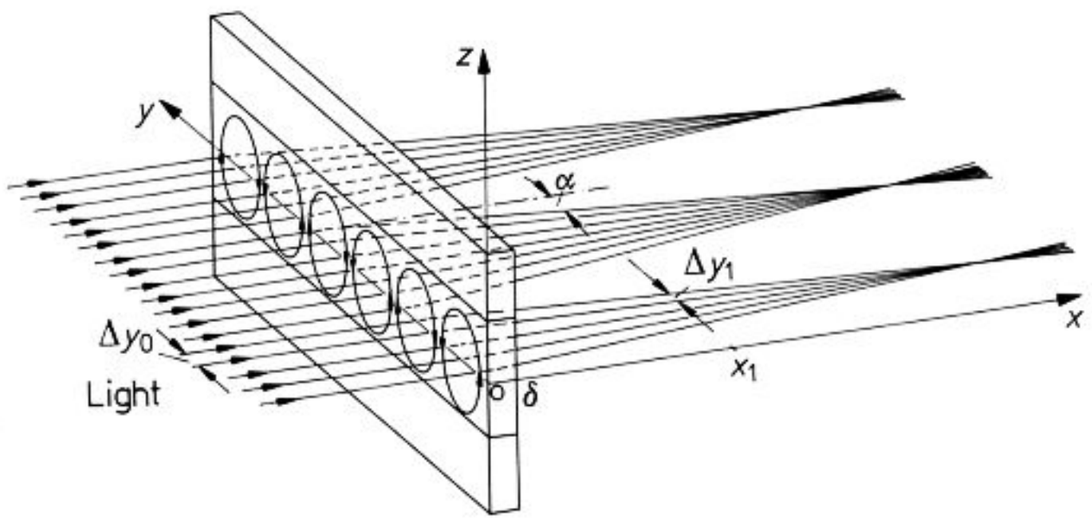

Fig. 1. Principle of the shadowgraph method: The incoming parallel light is deflected according to the gradient of the refraction index; δ is the thickness of the cell, α the maximum deflection angle of the light; at the observation line $x = x_1$ the intensity is modulated because the light sheet of thickness Δy_0, bounded by y_{01} and y_{02}, is transformed into a sheet of thickness $\Delta y_1 = y_{11} - y_{12}$; the transformation from y_{01} to y_{11} and y_{02} to y_{12} is given by Eq. (6)

2 Thermal convection

If a horizontal liquid layer is heated from below, convection rolls arise above a critical temperature gradient. The generated horizontal temperature gradient close to the critical point is proportional to a sine. Light which is sent from the side through the cell is deflected in a horizontal direction at this temperature gradient. The shadowgraph method applied to thermal convection therefore yields information about the temperature field of the flow. How to get the absolute temperature gradient from the observed shadowgraph pattern is shown in this chapter. The pattern is calculated at the line $x = x_1, z = 0$ (Fig. 1) where the light intensity is measured.

2.1 The path of the light for thermal convection

The coordinate system used for the calculations is shown in Fig. 1. The temperature in the x-direction is assumed to be constant. The y-dependence is $T = T_0 + \hat{T} \cdot \cos(k \cdot y)$ with k being the wave number of the convection pattern, and $\hat{T}$ the amplitude of the temperature variation stemming from the convection. Close to the middle of the cell where the z-dependence is $\partial \hat{T}/\partial z = 0$ the problem can be treated as one-dimensional. The relationship between density and temperature is $p = p_0 \cdot (1 - (T - T_0) \cdot \gamma)$ with γ being the thermal expansion coefficient. With the index of refraction being proportional to the density, the y-dependence is given by $n(y) = n_0 - \hat{T} \cdot n_0 \cdot \gamma \cdot \cos(k \cdot y)$. The principle of Fermat, $\int n \mathrm{d}s = \text{extremum}$, leads to the Euler-Lagrange equation (1) for the path of the light beam $y(x)$ in the cell

$$C \cdot (1 + y'^2)^{1/2} = n(y). \tag{1}$$

We expand this equation up to second order terms in $y(x) - y(0)$, its derivative y' and the derivative of the index of refraction. This approximation holds for small horizontal temperature gradients which is fulfilled close to the onset of convection. This means that we can only calculate the path in the cell for small deflections between in- and outgoing light beams. The constant C is determined by the boundary condition $y'(0) = 0$ for a perpendicular light beam and becomes $C = n(y_0)$ where $y_0 = y(0)$. With a Taylor expansion for n and the lhs of Eq. (1) we get in second order:

$$n(y_0) + \left.\frac{\partial n}{\partial y}\right|_{y_0} \cdot (y - y_0) = n(y_0) \cdot (1 + \tfrac{1}{2} \cdot y'^2). \tag{2}$$

Separation of the variables and integration leads to:

$$y(x) = \left.\frac{\partial n}{\partial y}\right|_{y_0} \cdot \frac{x^2}{2n(y_0)} + y_0. \tag{3}$$

To determine the light intensity at x_1 we need the angle of the light beam at $x = \delta$. We get

$$\tan(\alpha) = y'(\delta) = \left.\frac{\partial n}{\partial y}\right|_{y_0} \cdot \frac{\delta}{n(y_0)}. \tag{4}$$

Inserting the expressions for $n(y_0)$ and $\left.\frac{\partial n}{\partial y}\right|_{y_0}$ in Eq. (4) leads to:

$$\tan(\alpha) = \frac{\delta \cdot \hat{T} \cdot \gamma \cdot k \cdot \sin(k y_0)}{1 - T \cdot \gamma \cdot \cos(k y_0)} \cong \delta \cdot \gamma \cdot k \cdot \hat{T} \cdot \sin(k \cdot y_0) + \tfrac{1}{2} \cdot \delta \cdot \gamma^2 \cdot k \cdot \hat{T}^2 \cdot \sin(2 \cdot k \cdot y_0). \tag{5}$$

The second term on the rhs of Eq. (5) is much smaller than the first term because close to the critical point $\hat{T} \cdot \gamma$ is small (for a fluid layer of thickness 10 mm in the range of 10^{-4}). Therefore we take for the angle of deflection furthermore only the sine term of Eq. (5). Now we can calculate the light intensity at a distance x_1 from the cell.

2.2 Calculation of the light intensity at a distance x_1

The light intensity I at $x = 0$ is assumed to be $I_0 = \text{constant}$. The light intensity at the observation line $x = x_1$ (Fig. 1) is proportional to the ratio between the plane Δy_0 at $x = 0$ and its transformed plane Δy_1 at $x = x_1$. The transformation from Δy_0 to Δy_1 is composed of the light path inside the cell and the deflection with the angle α at $x = \delta$ to x_1. The shadowgraph pattern has been measured at a distance x_1 from the cell being large compared with the thickness $\delta (x_1 \gg \delta)$. Therefore we can neglect the small distortion inside the cell. With the calculated deflection angle from Eq. (5) close to the critical point, the transformation of y_0 to $y_1 = y(x_1)$ is given by:

$$y_1 \cong y_0 + \delta \cdot \gamma \cdot k \cdot \hat{T} \cdot x_1 \cdot \sin(k y_0) = y_0 + \alpha_0 \cdot x_1 \cdot \sin(k y_0). \tag{6}$$

The light intensity is proportional to $\Delta y_0 / \Delta y_1$. With $y_0 = f(y_1)$ being the inverse function from Eq. (6) we get for the light intensity at the point of observation

$$I(x_1, y_1) = I_0 \cdot \left(\frac{\partial y_1}{\partial y_0}\right)^{-1} = \frac{I_0}{1 + \alpha_0 \cdot x_1 \cdot k \cdot \cos(k \cdot f(y_1))}. \tag{7a}$$

$f(y_1)$ cannot be calculated analytically. We get the inverse function of Eq. (6) numerically with a Newton-Raphson method. Some intensity functions calculated with Eq. (7a) are shown in Fig. 2.

The denominator of Eq. (7a) can be zero for $x_1 \geq \frac{1}{\alpha_0 \cdot k}$. At $x_1 = \frac{1}{\alpha_0 \cdot k}$ we get the first caustic, a point with infinite intensity at $k \cdot f(y_1) = (2n + 1) \cdot \frac{\pi}{2}$. Above this distance Eq. (7a) has at least two points of infinite intensity within one period. The location of these singularities in the $x - y$-plane is shown in Fig. 3.

For finite diodes the singularities along the caustic lines change into points of high intensities. If we take into account the thickness Δ of the diode we get for the light intensity

$$I_\Delta(x_1, y_1) = \frac{1}{\Delta} \cdot \int_{y_1 - \Delta/2}^{y_1 + \Delta/2} I(x_1, y_1)\, dy_1 = I_0 \cdot \frac{1}{\Delta} \cdot (f(y_1 + \Delta/2) - f(y_1 - \Delta/2)), \tag{7b}$$

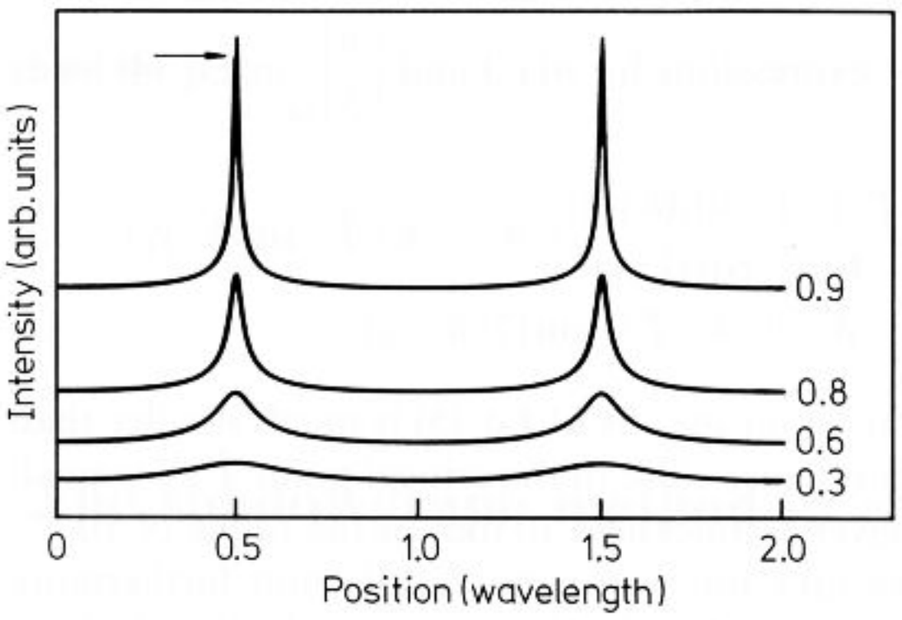

Fig. 2. Intensity lines for an infinitely thin and for a finite diode ($\Delta = 0.01$) according to the Eqs. (7a) and (7b); the parameter is the distance x_1 given in units of the distance from the first caustic; for values up to $x_1 = 0.8$ the difference between the two lines is smaller than 1%, making the second line invisible; at $x_1 = 0.9$ the difference becomes visible; the arrow points to the maximum of the intensity obtained with the finite diode size

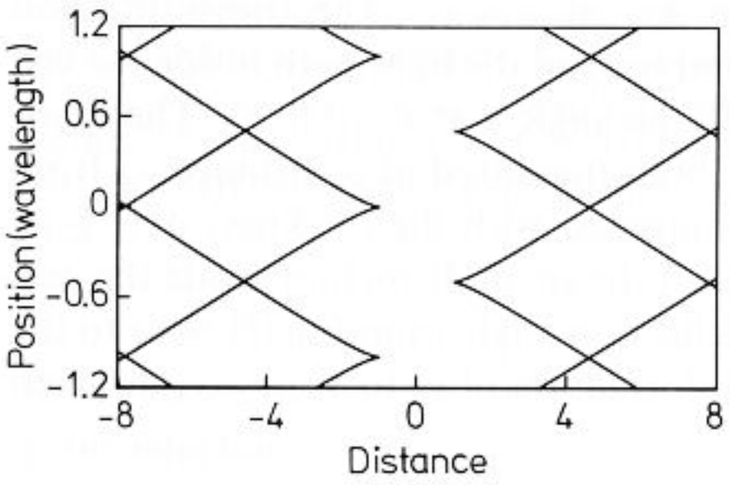

Fig. 3. The location of the singularities of Eq. (7a) in the $x-y$-plane are indicated by solid lines; the position along the cell is measured in units of the wavelength, the position along the x-direction in units of the distance between cell and first caustic; the focal points on the right hand side correspond to the real ones; focussing on the imaginary images on the left hand side with lenses might save space in the experimental setup; measuring the distance between the real and imaginary focal points gives quantitative information about the refractive index field (Fig. 15)

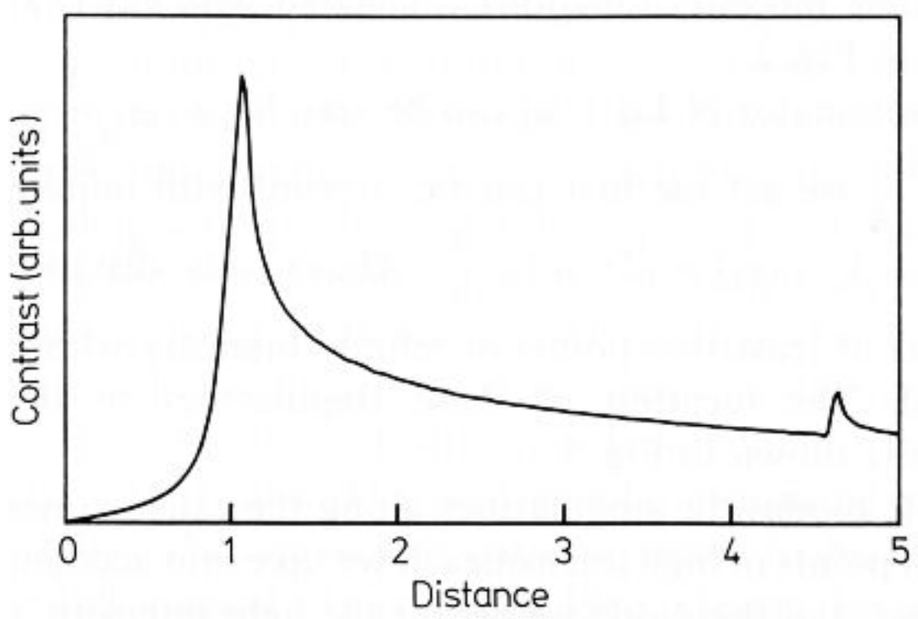

Fig. 4. The contrast $I_{max} - I_{min}$ in dependence on the distance between the observation line and the cell; the distance is scaled by the distance between the cell and the first caustic at $x_1 = 1$; using a finite diode, the thickness leads to a maximum of contrast at a position x_1 slightly larger than 1; the second peak at $x_1 = 4.7$ is caused by the crossing of two caustic lines (Fig. 3)

where we have assumed the sensitivity of the diode to be contant within the whole thickness Δ. The shape of the light intensity for different distances x_1 behind the threshold is also included in Fig. 2. It has been calculated with Eq. (7b) with $\Delta = 0.01$ and a wavelength of 1. There is no visible difference, however, between the intensities obtained with an infinitely small diode (7a) and the one obtained by a diode of thickness 0.01, provided that the observation line is far enough from the first focal point. Thus Eq. (7a) can be used to fit the experimental data.

Especially for the wavelength measurements of the convection patterns it is important to get a high contrast of the image. Figure 4 shows the contrast defined as the difference between the maximum and the minimum intensity as a function of the distance from the cell. It can be seen that the ideal distance x_1 is close to the first caustic.

In the experimental part Eq. (7a) will be used to fit the experimental data. From the parameter α_0 we cant get the temperature gradient in horizontal direction of the cell. A comparison of the parameter α_0 with Eq. (5) yields $\alpha_0 = \delta \cdot \gamma \cdot k \cdot \hat{T}$. If we take into account the refraction of the light beam at the transition from liquid to air at $x = \delta$ the amplitude of the temperature modulation with a mean index of refraction $\bar{n}$ of the fluid would be:

$$\hat{T} = \alpha_0 \cdot (k \cdot \gamma \cdot \delta \cdot \bar{n})^{-1}. \tag{8}$$

2.3 Experimental examples for thermal convection

The experimental data for the first two experiments described here in have been obtained by using photodiodes moved along the x-direction at $z = 0$ (Fig. 1). The photovoltage is proportional to the light intensity.

Thermal convection in a channel with "ramped boundaries" leads to almost perfect selection of the wavelength of the convection rolls. The detailed geometry of our convection channel (3 mm high, 1.5 mm thick, 24 mm long) is given elsewhere (Rehberg et al. 1987). Purified cyclohexan was used as the working fluid in this experiment. To obtain the wavelength and the critical temperature we measured the light intensity at a distance of 70 cm behind the cell. A photodiode, moved along the x-axis by means of a stepping motor, measures the light intensity. First the intensity is measured in the absence of convection – this intensity profile is then used to normalize the other measurements, thus getting rid of light inhomogeneities. The measured light intensities together with a least square fit to Eq. (7a) is shown in Fig. 5. The deflection angle α_o obtained from this fit shows the expected square root dependence close to the critical point as indicated in Fig. 6. The wavelength obtained from the fit is presented elsewhere (Rehberg and Riecke 1987).

The second experiment deals with convection patterns in two horizontal layers of immiscible liquids lying one upon the other (Rasenat 1987). Details of the experimental setup will be given elsewhere (Rasenat et al. 1989). The dimensions of the convection box are 12 mm · 20 mm · 80 mm. A 6 mm layer of ethyleneglycol was covered with a 6 mm layer of oil.

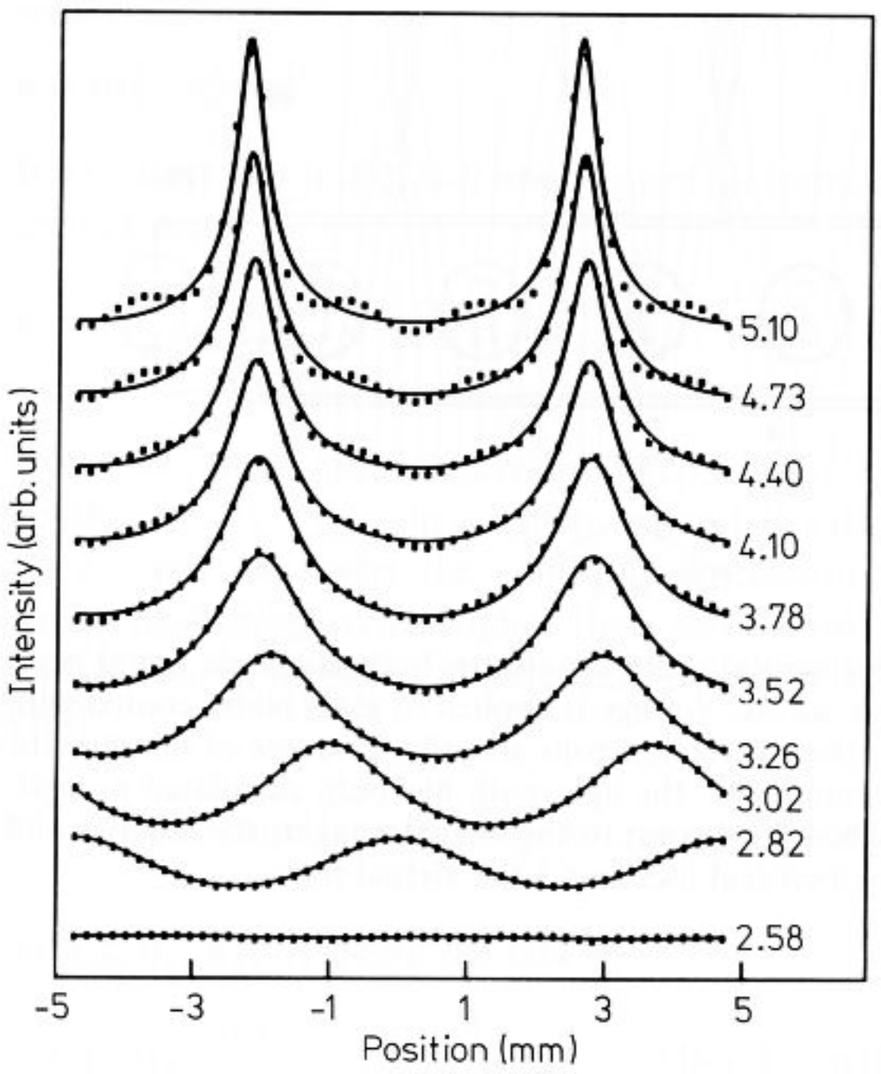

Fig. 5. Shadowgraphic image of convection rolls in a "ramped" convection channel; the labels indicate the temperature difference between top and bottom; the points are measurements obtained by a photodiode, the solid line is a fit to Eq. (7a); the fit appears satisfactorily up to about 4 K, but above this temperature difference higher harmonics appear

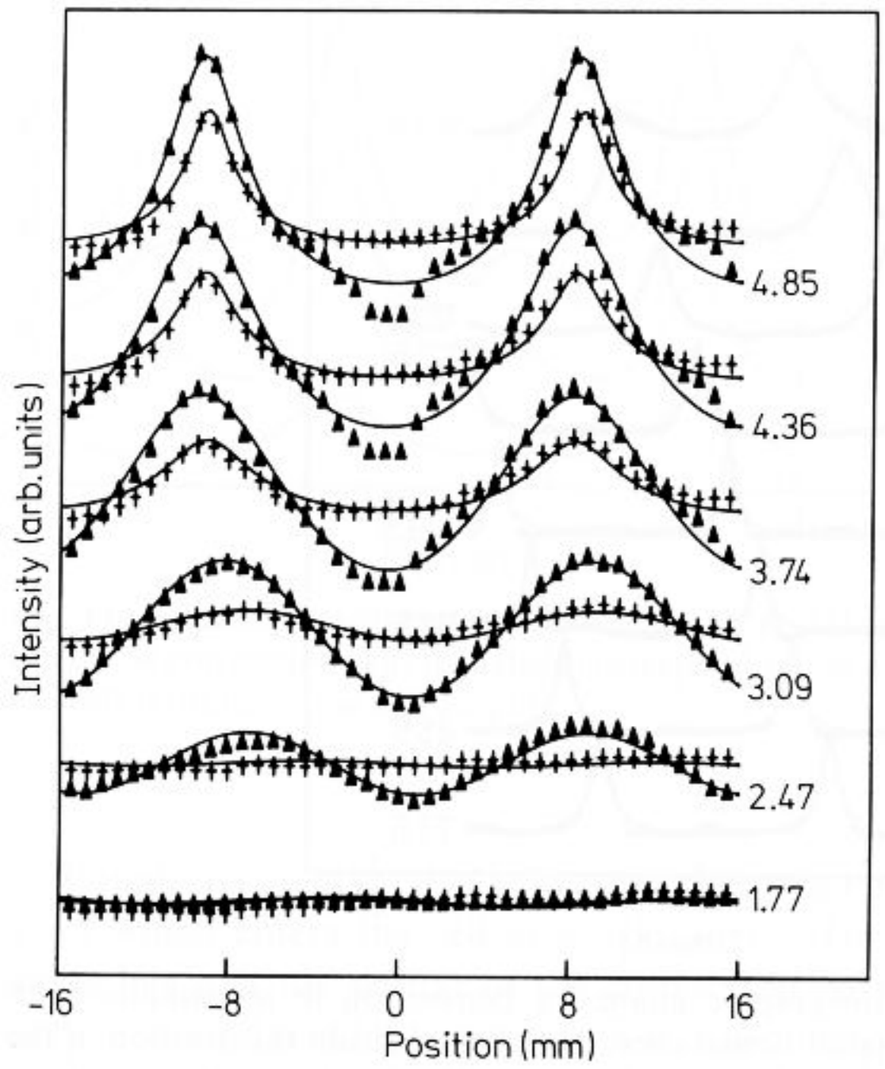

Fig. 7. Shadowgraphic image of double layer convection; the triangles are measurements in the upper oil layer, the crosses are obtained from measurements in the lower layer of ethyleneglycol; the parameter is the temperature difference (K) between the top and bottom plate

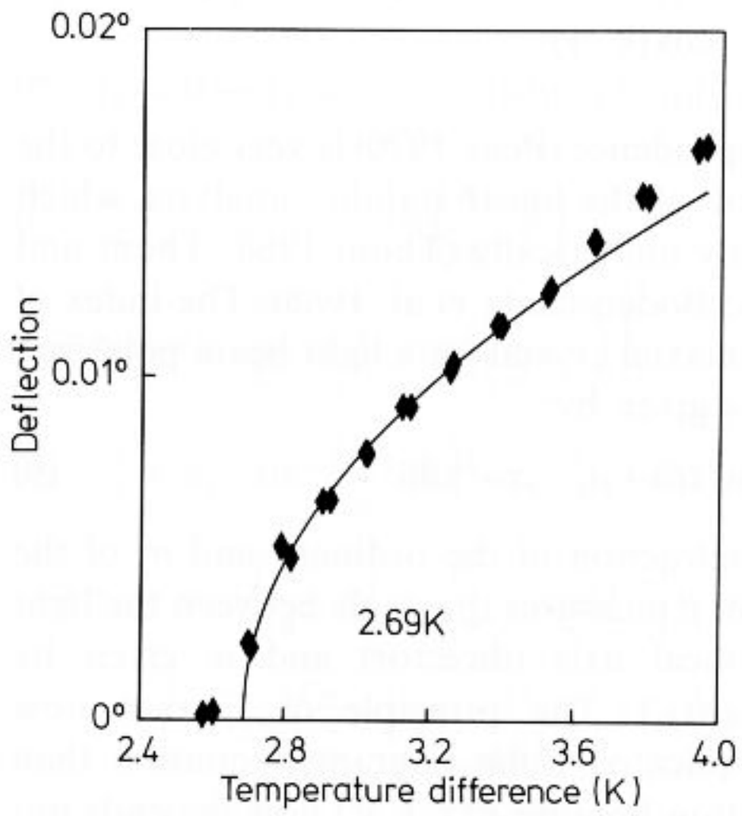

Fig. 6. The deflection angle in dependence on the temperature difference as extracted from Fig. 5; the solid line is a fit to a square root law

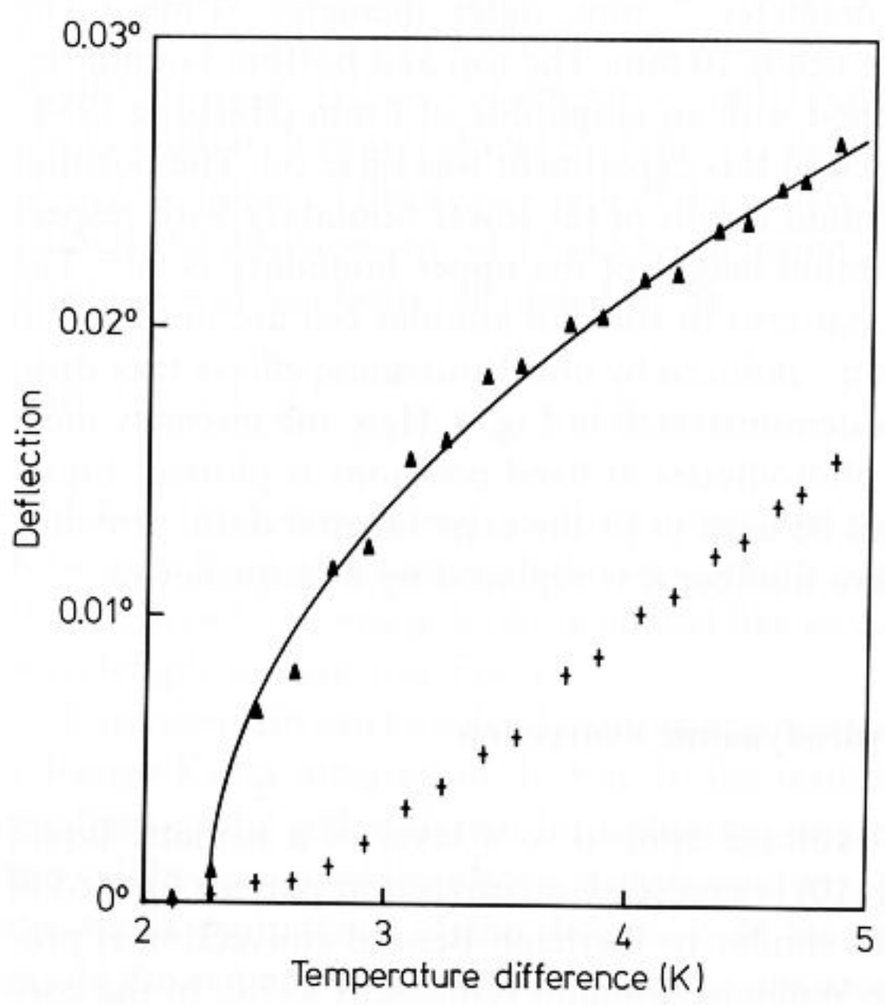

Fig. 8. The deflection angle in dependence on the temperature difference as extracted from Fig. 7; the solid line is a fit to a square root law

The same procedure as in the first experiment was used to obtain intensity measurements, with the only difference that two diodes were used instead of one. Figure 7 presents the intensities obtained by the two diodes. Separated convection rolls appear in both layers. The deflection angle α_0 in dependence on the temperature difference (Fig. 8) shows a square root dependence for only the layer that gets first unstable. The other one is only passively driven at the beginning of convection, thus the light intensity modulation is very small here. For ethyleneglycol a deflection angle of 0.01° corresponds to a horizontal temperature modulation with an amplitude $\hat{T}$ of 0.02 K.

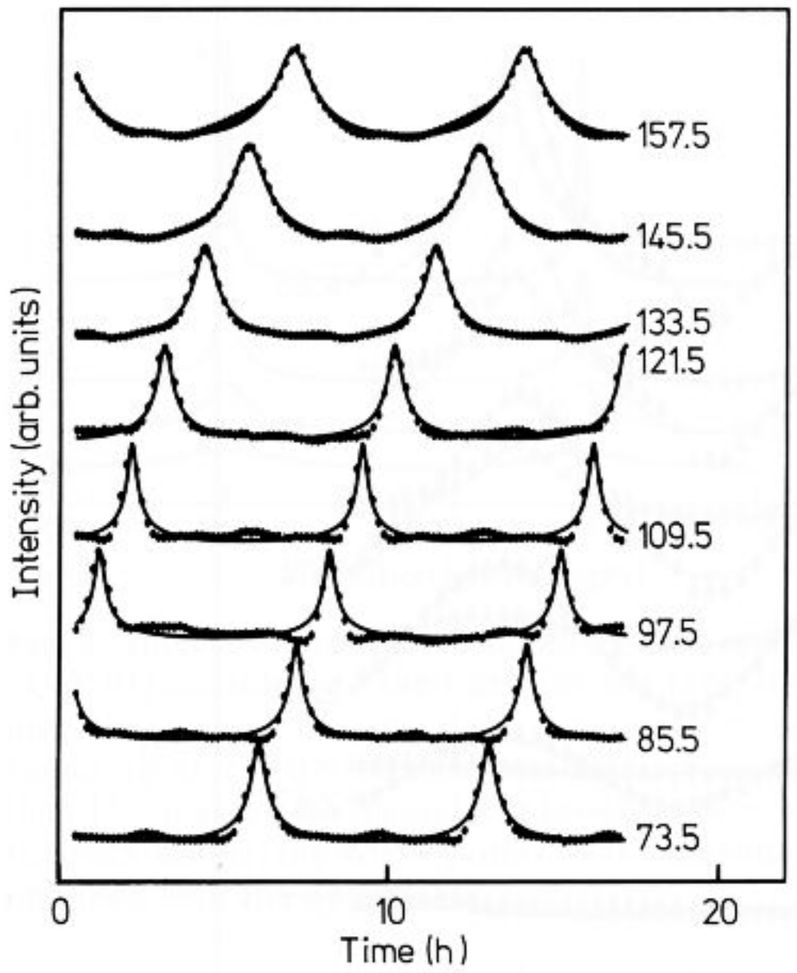

Fig. 9. Shadowgraphic image for convection in an annulus with harmonic spatial boundaries; the labels indicate the position of the measuring photodiode in degrees with respect to the maximum height of the upper boundary; the maximum height of the lower boundary is at 90°

The third experiment deals with convection in an annular cell (inner diameter 22 mm, outer diameter 31 mm.) The height of the cell is 10 mm. The top and bottom boundaries are sine shaped with an amplitude of 1 mm (Hartung 1988). The fluid used in this experiment was olive oil. The position of the maximum height of the lower boundary with respect to the maximum height of the upper boundary is 90°. The convection patterns in such an annular cell are not fixed in their position – induced by non-Boussinesq effects they drift. This drift is demonstrated in Fig. 9. Here the intensity measured by 8 photodiodes at fixed positions is plotted. Equation (7 a) can be used to fit the experimental data, provided that the wave number k is replaced by a frequency ω.

3 Electrohydrodynamic convection

If a critical voltage applied to a layer of a nematic liquid crystal (Fig. 10) is exceeded, a convection pattern formed of parallel rolls similar to Rayleigh-Bénard convection is produced – the Williams domains (Goossens 1978). In the convective state the velocity field in the layer and the director angle are spatially periodic with the same wavelength. From an optical point of view a nematic is an uniaxial crystal showing birefringence (Born 1932). Light polarized in the direction of the director is deflected when passing the cell (Penz 1970; Hirata and Tako 1982). A microscope focussed to a plane close above the liquid is used to visualize the resulting shadowgraph image. How to get the distortion angle of the director form this image is shown in this section.

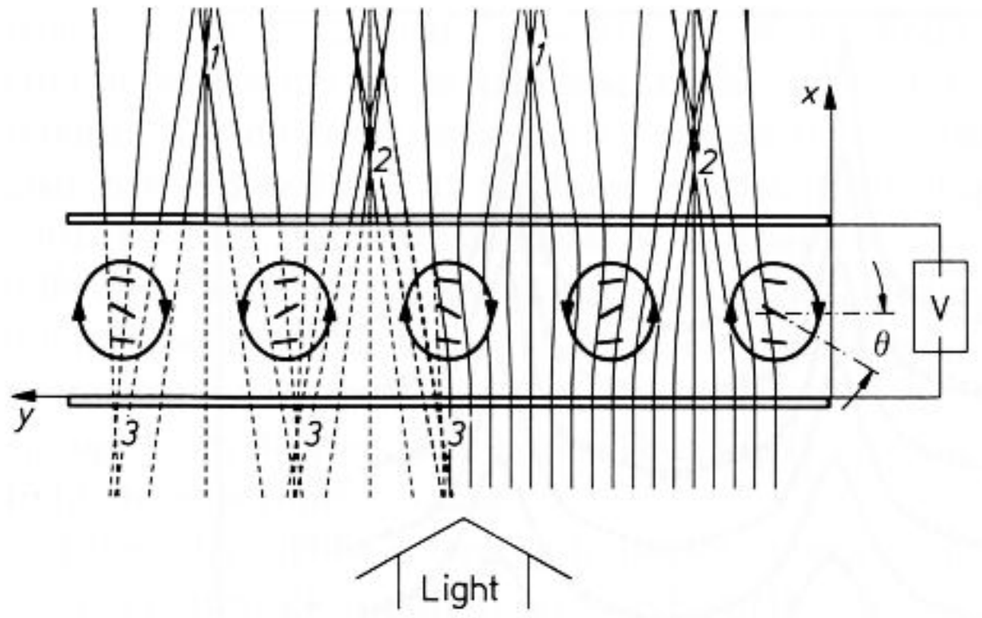

Fig. 10. Experimental setup for electro-hydrodynamic liquid crystal convection; an AC-voltage is applied to glass plates coated with a conductor; the convection rolls and the tilt angle of the director is shown schematically; the light path has been calculated numerically; the dashed lines point to the virtual images; the labels 1 and 2 indicate the two real foci and 3 the virtual focus

3.1 The path of the light in liquid crystals

A model of the cell is shown in Fig. 10. To derive some analytic results of the path of the light $y(x)$ passing the cell, we will use a simplified model for the angle θ of the director (Fig. 10), namely

$$\theta = \theta_0 \cdot \sin\left(\frac{\pi}{\delta} \cdot x\right) \cdot \cos(k \cdot y) .$$

This simple y-dependence (Penz 1970) is very close to the correct eigenfunction of the linear stability analysis, which can be obtained only numerically (Thom 1988; Thom and Zimmermann 1988; Bodenschatz et al. 1988). The index of refraction n in an uniaxial crystal for a light beam polarized in the $x-y$-plane is given by:

$$n(x, y, y') = (n_0^2 \cdot \sin^2(\beta) + n_e^2 \cdot \cos^2(\beta))^{1/2} . \tag{9}$$

n_0 is the index of refraction of the ordinary and n_e of the extraordinary beam. β measures the angle between the light beam and the optical axis (director) and is given by $\beta = -\theta(x, y) + \arctan(y')$. The principle of Fermat now yields a more complicated Euler-Lagrange equation than for thermal convection because $n(x, y, y')$ now depends not only on x but also on y and its first derivative y':

$$\frac{\partial f}{\partial y} - \frac{\partial^2 f}{\partial y' \partial x} - \frac{\partial^2 f}{\partial y' \partial y} \cdot y' - \frac{\partial^2 f_2}{\partial y'} \cdot y'' = 0 \tag{10}$$

with $f(x, y, y') = n(x, y, y') \cdot (1 + y'^2)^{1/2}$. Again, we consider small amplitude convection in a small region above the critical point where θ and the deflection $y - y_0$ and its derivatives remain small. f is expanded into a Taylor series up to the second order in the small terms:

$$f \cong n_e \cdot \left(1 + \frac{1}{2} \cdot \hat{n} \cdot (y' - \theta)^2\right) + \frac{1}{2} \cdot n_e \cdot y'^2$$

with

$$\hat{n} = (n_0^2 - n_e^2)/n_e^2 \ .$$

If we insert this in Eq. (10) and neglect all terms higher than second order we get

$$\hat{n} \cdot \theta \cdot \frac{\partial \theta}{\partial y} + \hat{n} \cdot \frac{\partial \theta}{\partial x} - (\hat{n}+1) \cdot y'' = 0 \,. \tag{11}$$

Now we make use of $\cos(k\,y) = \cos(k\,y_0 - k\,(y_0 - y)) \cong \cos(k\,y_0) - k\,(y - y_0) \cdot \sin(k\,y_0)$ to expand θ with respect to $y - y_0$, and we insert the resulting expression in Eq. (11). Again neglecting terms higher than second order we get a linear, inhomogeneous differential equation of the Hill's kind

$$z'' = \theta_0^2 \cdot a_1 \cdot \sin^2\left(\frac{\pi}{\delta} \cdot x\right) - \theta_0 \cdot z \cdot a_3 \cdot \cos\left(\frac{\pi}{\delta} \cdot x\right), \tag{12}$$

with z, a_1, a_2, a_3 being defined by

$$z = y - y_0 - \frac{a_2}{a_3}, \quad a_1 = \frac{\hat{n}}{1+\hat{n}} \cdot k \cdot \cos(k\,y_0) \cdot \sin(k\,y_0)\,,$$

$$a_2 = \frac{\hat{n}}{1+\hat{n}} \cdot \frac{\pi}{\delta} \cdot \cos(k\,y_0)\,, \qquad a_3 = \frac{\hat{n}}{1+\hat{n}} \cdot \frac{\pi \cdot k}{\delta} \cdot \sin(k\,y_0)\,.$$

To solve Eq. (12), we make a series ansatz for z up to second order terms in θ_0: $z = z_1 + \theta_0 \cdot z_2 + \theta_0^2 \cdot z_3$. Inserting this in Eq. (12) we get for the different orders:

$$\theta_0^0\text{: } z_1'' = 0 \to z_1 = -\frac{a_2}{a_3} \quad \text{(which fulfills } y(0) = y_0,\ y'(0) = 0).$$

$$\theta_0^1\text{: } z_2'' = -z_1 \cdot a_3 \cdot \cos\left(\frac{\pi}{\delta} \cdot x\right)$$

$$\to z_2 = a_2 \cdot \frac{\delta^2}{\pi^2} \cdot \left(1 - \cos\left(\frac{\pi}{\delta} \cdot x\right)\right).$$

$$\theta_0^2\text{: } z_3'' = a_1 \cdot \sin^2\left(\frac{\pi}{\delta} \cdot x\right) - z_2 \cdot a_3 \cdot \cos\left(\frac{\pi}{\delta} \cdot x\right)$$

$$\to z_3 = a_1 \cdot \left(\frac{1}{4} \cdot x^2 + \frac{\delta^2}{8\pi^2} \cdot \cos\left(\frac{2\pi}{\delta} \cdot x\right)\right) - a_2 \cdot a_3 \cdot \frac{\delta^4}{\pi^4}$$

$$\cdot \left(-\cos\left(\frac{\pi}{\delta} \cdot x\right) - \frac{\pi^2}{4\delta^2} \cdot x^2 + \frac{1}{8} \cdot \cos\left(\frac{2\pi}{\delta} \cdot x\right)\right) + C$$

with

$$C = -a_1 \cdot \frac{\delta^2}{8\pi^2} - \frac{7}{8} \cdot a_2 \cdot a_3 \cdot \frac{\delta^4}{\pi^4}\,.$$

The solution $y(x)$ up to the second order in θ_0 is then: $y(x) = y_0 + \theta_0 \cdot z_2 + \theta_0^2 \cdot z_3$. To calculate the deflection angle α at $x = \delta$ we need the first derivative of $y(x)$ at $x = \delta$. We get:

$$y'(\delta) = \tan\alpha = \theta_0^2 \cdot \frac{\hat{n}}{1+\hat{n}} \cdot \frac{1}{4} \cdot k \cdot \delta \cdot \left(-1 + \frac{\hat{n}}{1+\hat{n}}\right) \cdot \sin(2k\,y_0)\,. \tag{13}$$

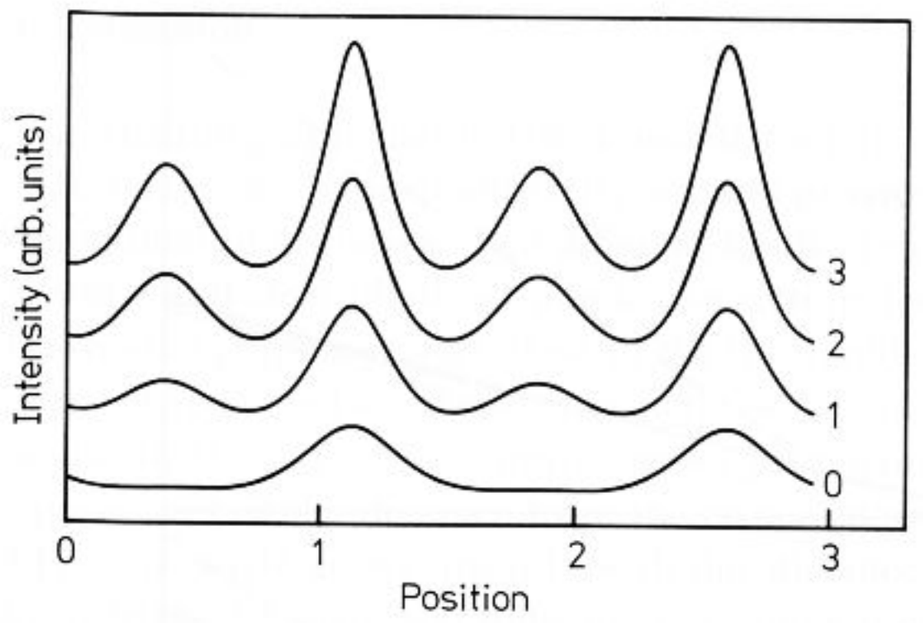

Fig. 11. Intensity calculated as a function of the distance from the top of the convection cell; the labels correspond to the distance from the cell in units of the cell height

Equation (13) gives the deflection angle of a light beam at $x = \delta$ which enters the cell at $x = 0$ and y_0. The deflection angle has half the period of the convection pattern and is only in second and higher orders in θ_0 unequal to zero. This result is not surprising because the dependence on the index of refraction is only quadratic to the angle between the light beam and the optical axis (axis of the director), i.e., there is no difference between negative and positive angles of the director [Eq. (9)]. If only the deflection angle is taken into account, this simplified analysis would predict the image of the convection pattern to be half the wavelength of the actual convection – a fact which sometimes produced wrong results for measurements of the wavelength (Penz 1970). The above analysis however shows that there is also a linear term giving the image of the wavelength of the convection pattern, namely the displacement of a light beam inside the cell. This displacement has been calculated to be

$$y(\delta) - y_0 = 2 \cdot \theta_0 \cdot \frac{\hat{n}}{1+\hat{n}} \cdot \frac{\delta}{\pi} \cdot \cos(k\,y_0)$$

and has the same period as the convection pattern. The transition from an image with the wavelength of the convection pattern to an image looking almost like having half this wavelength is shown in Fig. 11.

Equation (10) can be solved without approximations with a Runge-Kutta integration. In Fig. 10 the resulting path of the light in the cell is shown for a director angle exceeding the validity range of the above approximations. We can see the single periodicity of the deflection of the light beams inside the cell and two real foci in similar distances from the cell.

The distances between the foci can be calculated. The transformation for y from $x = 0$ to $x = x_1$ is given by $y_1 = y(\delta) + y'(\delta) \cdot (x_1 - \delta)$ which yields for the intensity at $x = x_1$

$$I = \frac{I_0}{\left(\dfrac{\partial y(\delta)}{\partial y_0} + (x_1 - \delta) \cdot \dfrac{\partial y'(\delta)}{\partial y_0}\right)}\,. \tag{14}$$

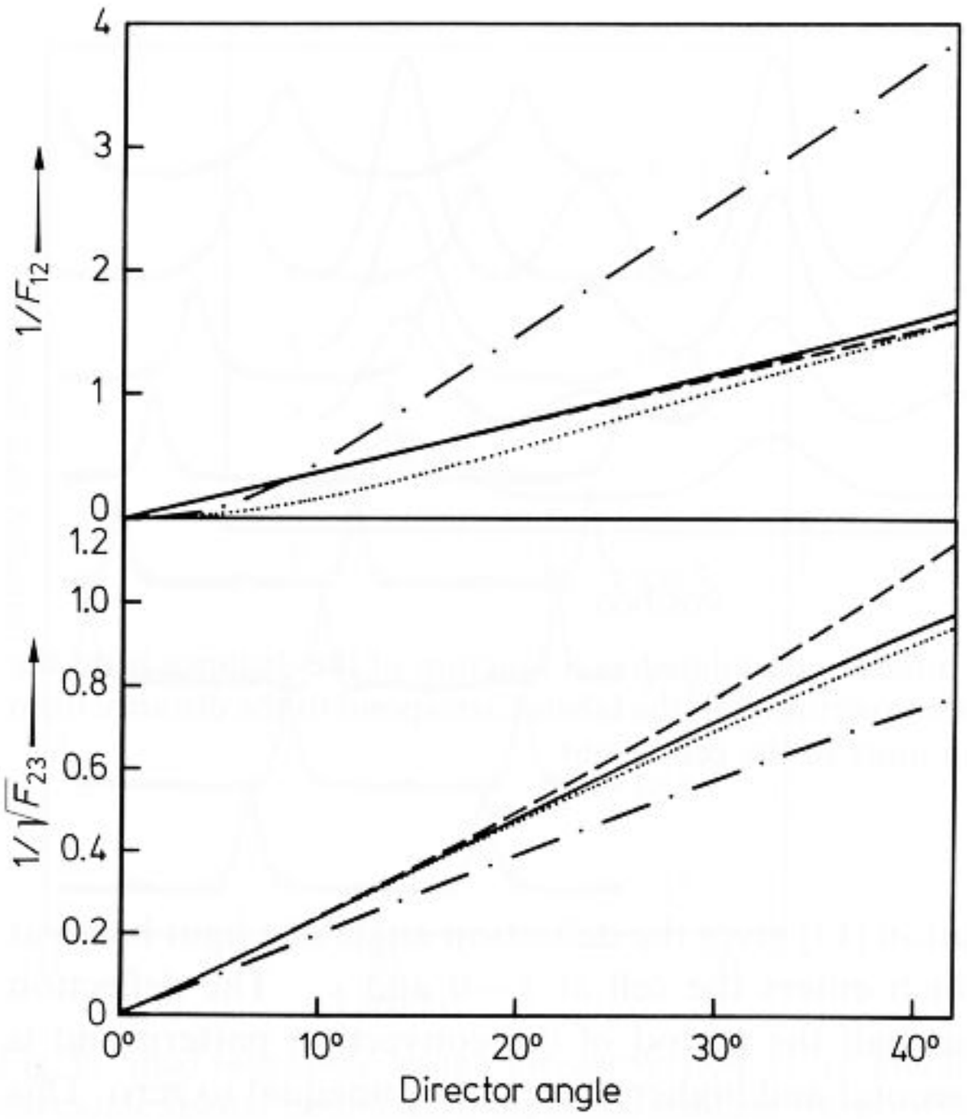

Fig. 12. The distance between the two real foci 1 and 2, and the real and imaginary foci 2 and 3 as a function of the director angle; the dashed lines belong to a sine as eigenfunction for the director angle in x-direction with approximation for small angles and the solid lines without approximation for the same eigenfunction; the dashed dotted lines belong to an eigenfunction of Thom (1988) and the dotted lines to an eigenfunction of Bodenschatz (1988)

The first caustics are at minimum distances x_1 where the denominator of Eq. (14) becomes zero. The analytical calculations with the above equations for $y(x)$ and $y'(x)$ yields for the distances between the planes of the real caustics (2) and the virtual caustics (3)

$$F_{23} = \frac{4}{\theta_0^2 \cdot N \cdot k^2 \cdot \delta \cdot (N-1)} + \frac{4}{\theta_0 \cdot \pi \cdot k \cdot (N-1)} \,. \tag{15}$$

The distances between the planes of the two real caustics is:

$$F_{12} = \frac{8}{\theta_0 \cdot \pi \cdot k \cdot (N-1)} \qquad \text{with } N = \frac{\hat{n}}{1+\hat{n}} \,. \tag{16}$$

The inverse of the square root of F_{23} and the inverse of F_{12} are shown in Fig. 12 (dashed lines). The solid lines in this picture have been calculated with the numerical solution of Eq. (10) obtained by the Runge-Kutta integration.

If we take the x-dependence of the director angle as not being a sine (as given by the Penz model) but rather the correct solution obtained by a linear stability analysis at the threshold (Thom 1988; Bodenschatz et al. 1988) we get the dashed-dotted (Thom 1988) or the dotted lines (Bodenschatz et al. 1988) in Fig. 11. The two curves differ in the parameters assumed for the liquid crystal (the parameter sets MBBA I and MBBA II in Bodenschatz et al. 1988). The distance between the two real focal points seems to be especially sensitive against variations of these parameters.

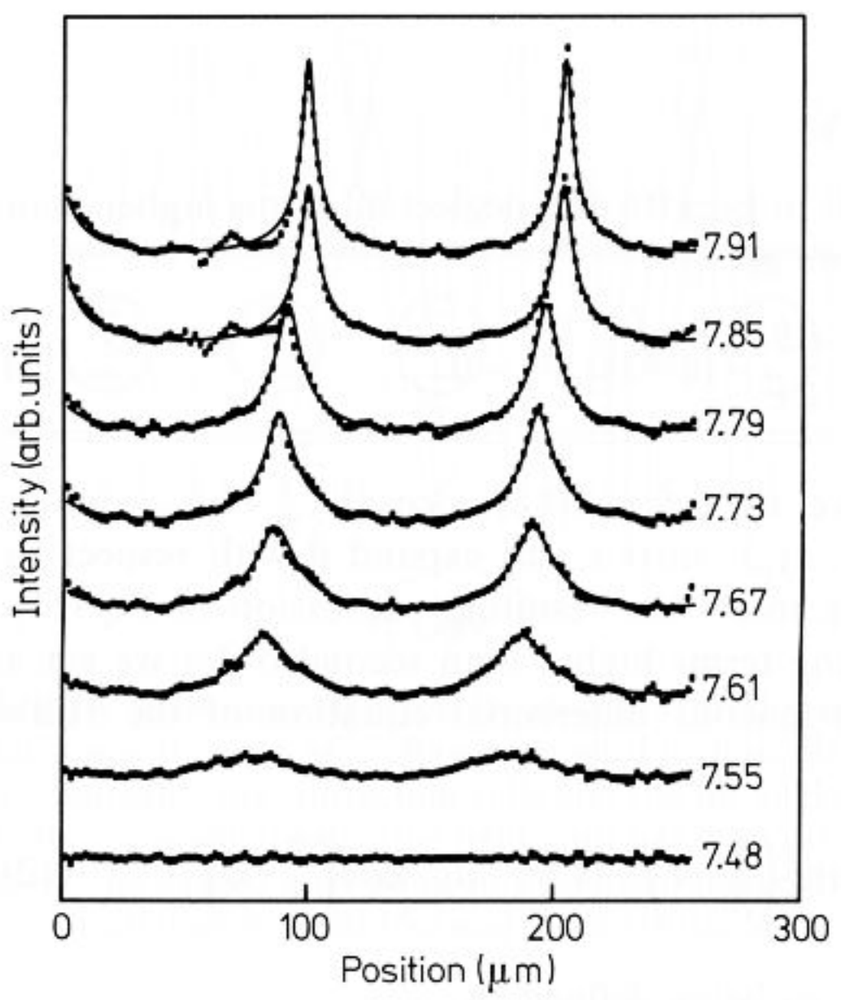

Fig. 13. Intensity measured at the top of the cell for MBBA corresponding to a cutoff frequency of 600 Hz; the cell height is 100 μm; labels indicate the RMS-voltage applied with a frequency of 107 Hz

3.2 Experimental example for electrohydrodynamic convection

For small deflections the path of the light beam inside the liquid crystal layer can be approximated by a straight line forming an angle α with the x-axis. Using this approximation we can calculate the shadowgraph picture at the upper boundary of the layer in the same way as in Sect. 2.2. The angle α corresponds to

$$\alpha \cong (y(\delta) - y_0)/\delta = 2 \cdot \theta_0 \cdot \frac{\hat{n}}{1+\hat{n}} \cdot \frac{1}{\pi} \cdot \cos(k\, y_0)$$
$$= \alpha_0 \cdot \cos(k\, y_0) \,.$$

By fitting the function (7a) at shadowgraph pictures of electrohydrodynamic convection we can get from the parameter α_0 the amplitude of the angle of the director:

$$\theta_0 = \alpha_0 \cdot \frac{\pi}{2} \cdot \frac{1+\hat{n}}{\hat{n}} \,. \tag{17}$$

Experimental data obtained close to the top of the cell and the fitted function for different voltages are shown for a liquid crystal layer (MBBA) of 100 μm thickness in Fig. 13. The shape of the curves is the same as in the case of thermal convection (Fig. 5) which indicates the accuracy of the considerations we made for liquid crystals in Sect. 3.1.

The fit shown in Fig. 13 in principle contains the information about the director angle, provided that the focal plane of the microscope is known exactly with respect to the upper boundary of the cell. With clean electrodes the exact determination of the position of the plane might become difficult. Thus in Fig. 14 we have only shown the deflection angle in

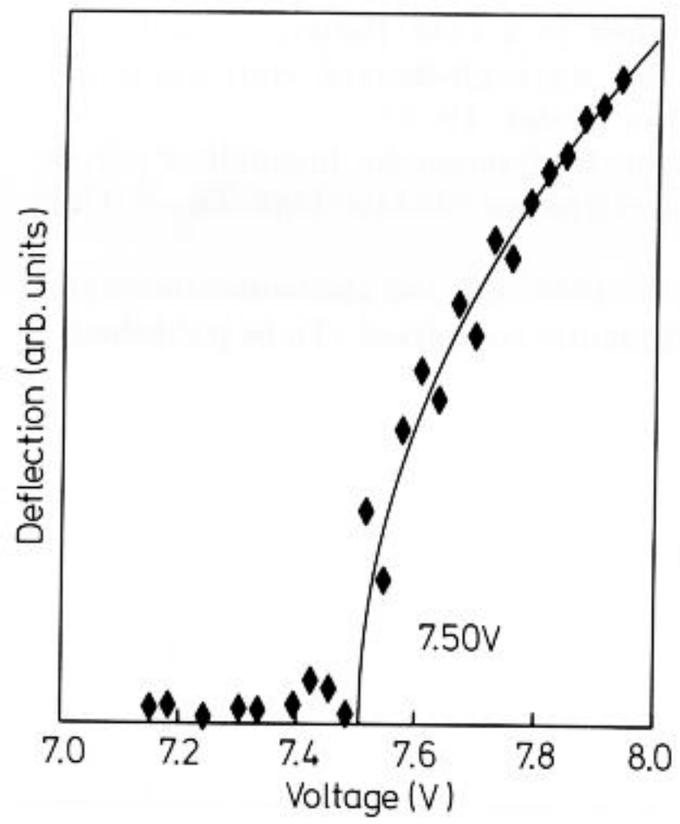

Fig. 14. The deflection angle of the light as extracted from Fig. 13; the solid line is a fit to a square root law giving a critical voltage of 7.5 V

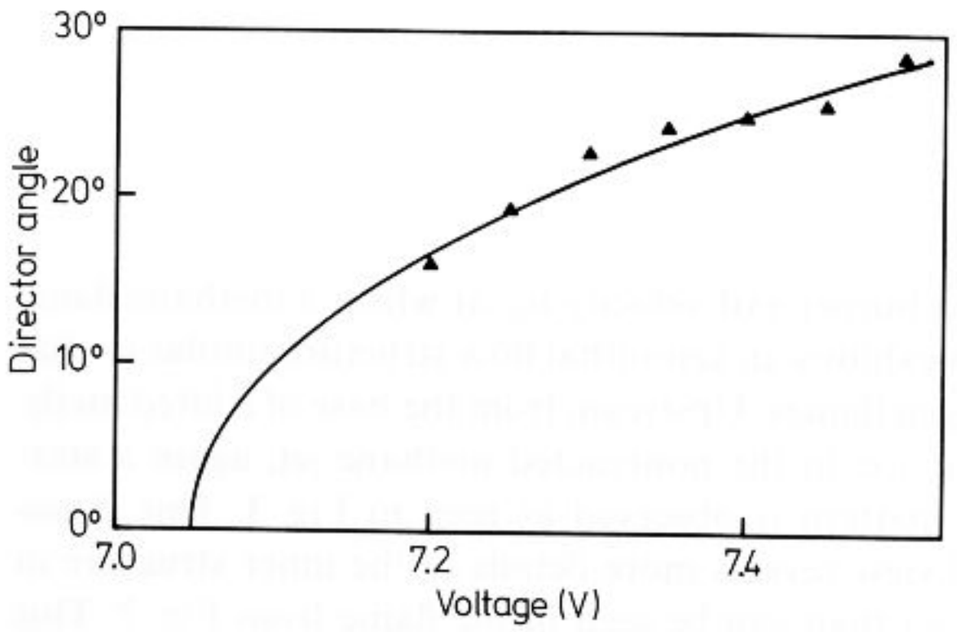

Fig. 15. The director angle measured in a 23 μm cell filled with MBBA having a cutoff frequency of approximately 160 Hz; the difference between the real and virtual foci are measured; the solid line is the theoretical curve obtained from a nonlinear perturbation expansion

arbitrary units, together with a fit to the expected square root law behaviour.

A simple way to avoid the difficulty in absolute positioning is to measure a relative length, namely the distance between the two focal planes 2 and 3 (Fig. 10). The director angle can be extracted from this measurement according to the function presented in Fig. 12. This has been done in Fig. 15. There is only a limited range where the procedure works satisfactorily. If the voltage is too small the caustics are hard to focalize, and for voltages too high, the time dependent motion of the convection pattern sets in. From the measurements a critical voltage at about 7.50 V can be extrapolated. The parabola shown in Fig. 15 is the theoretical curve according to a weakly nonlinear stability analysis (Bodenschatz et al. 1988).

4 Conclusion

The shadowgraph method is a useful tool in convection experiments even for quantitative aspects provided that the eigenfunction is known. Two different kinds of experiments, thermal and electrohydrodynamic convection, lead to similar shadowgraphic images close to the threshold. The difference between the two cases is the angle of the outgoing light beam. In thermal convection it grows proportional to the square root of the distance from the critical point, while in EHC this angle grows linearily with this distance. With this knowledge the shadowgraphic images can be used to extrapolate the critical point for the onset of convection with high precision.

Acknowledgements

It is a pleasure to thank E. Moses, V. Steinberg, E. Weißhaar and F. H. Busse for clarifying discussions, and W. Thom, E. Bodenschatz and W. Zimmermann for making the eigenfunctions of the linear stability analysis available to us prior to publication. This work was supported by Stiftung Volkswagenwerk, Minerva Foundation and the Deutsche Forschungsgemeinschaft through SFB 213 (Bayreuth).

References

Ahlers, G.; Cannell, D. S.; Steinberg, V. 1985: Time dependence of flow patterns near the convective threshold in a cylindrical container. Phys. Rev. Lett. 54, 1373

Blinov, L. M. 1983: Electro-optical and magneto-optical properties of liquid crystals. New York: Wiley

Bodenschatz, E.; Zimmermann, W.; Kramer, L. 1988: On electrically driven pattern-forming instabilities in planar nematics. J. Phys. 49, 1875–1899

Born, M. 1932: Optik, 3rd edn. Berlin: Springer

Busse, F. H. 1978: Non-linear properties of thermal convection. Rep. Prog. Phys. 41, 1929–1976

Busse, F. H. 1980: Transition to turbulence in Rayleigh-Bénard convection. In: Hydrodynamic instabilities and the transition to turbulence (eds. Swinney, H. L.; Gollub, J. P.). Berlin, Heidelberg, New York: Springer (Topics an applied physics, vol. 45)

Goossens, W. J. A. 1978: Electrohydrodynamic instabilities in nematic liquid crystals. In: Advances in liquid crystals (ed. Brown, G. H.). London: Academic Press

Hartung, G. 1988: Rayleigh-Bénard-Konvektion mit periodisch modulierten Randbedingungen. Dipl. Thesis. Univ. Bayreuth

Heutmaker, M. S.; Fraenkel, P. N.; Gollub, J. P. 1985: Convection patterns: Time evolution of the wave-vector field. Phys. Rev. Lett. 54, 1369

Hirata, S.; Tako, T. 1982: Optical properties of Williams domain. Jpn. J. Appl. Phys. 21, 675–579

Joets, A.; Ribotta, R. 1986: Hydrodynamic transitions to chaos in the convection of an anisotropic fluid. J. Phys. 47, 595–606

Kolodner, P.; Walden, R. W.; Passner, A.; Surko, C. M. 1986: Rayleigh-Bénard convection in an intermediate-aspect-ratio rectangular container. J. Fluid Mech. 163, 195–226

Lowe, M.; Albert, B. S.; Gollub, J. P. 1986: Convective flows with multiple spatial periodicities. J. Fluid Mech. 173, 253–272

Penz, P. A. 1970: Voltage-induced vorticity and optical focusing in liquid crystals. Phys. Rev. Lett. 24, 1405–1409

Pocheau, A.; Croquette, V.; Le Gal, P. 1985: Turbulence in a cylindrical container of Argon near threshold of convection. Phys. Rev. Lett. 55, 1094

Rasenat, S. 1987: Konvektion in zwei geschichteten Flüssigkeiten. Dipl. Thesis. Univ. Bayreuth

Rasenat, S.; Busse, F. H.; Rehberg, I. 1989: A theoretical and experimental study of double-layer convection. J. Fluid Mech. 199, 519–540

Rehberg, I.; Riecke, H. 1987: Rayleigh number ramps cause moving convection patterns. In: The physics of structure formation theory and simulation (eds. Güttinger, W.; Dangelmayr, G.). Berlin, Heidelberg, New York: Springer (Springer series synergetics, vol. 37)

Rehberg, I.; Bodenschatz, E.; Winkler, B. L.; Busse, F. H. 1987: Forced phase diffusion in a convection experiment. Phys. Rev. Lett. 59, 282–284

Steinberg, V.; Ahlers, G.; Cannell, D. S. 1986: Pattern formation and wave-number selection by Rayleigh-Bénard convection in a cylindrical container. Phys. Script. T9, 97

Thom, W. 1988: Die elektrohydrodynamische Instabilität mit Berücksichtigung des flexoelektrischen Effektes. Dipl. Thesis. Univ. Bayreuth

Thom, W.; Zimmermann, W. 1988: On the electrohydrodynamic instability in nematics: A picture completed. (To be published)

Received October 10, 1988

Technical notes

Azimuthal instability in jet diffusion flames

H. Eickhoff[1], A. Winandy[1] and R. Natarajan[2]

[1] DFVLR, Institut für Antriebstechnik D-5000 Köln 90, FR Germany
[2] Indian Institute of Technology, Madras, India

Transitional jet diffusion flames develop a structure of toroidal vortices, which result from the instability of the jet shear layer. In order to investigate the mechanism of transition in the initial flow regime of such flames, a visualization study of the flow structure in the inital region of the jet flames was perfomed with hydrogen and methane as the fuel. The burners were contured nozzles of 5 and 10 mm diameter and of contraction ratio 50:1 and 12.5:1, respectively. The flow structure was visualized by schlieren images and light sheets perpendicular to the flow axis. A nanolight served as the light source in a Toepler schlieren set-up, and for the light sheet visualization scattering particles were produced by atomizing water mixed with TiO_2-powder.

Toroidal vortices, resulting from the instability of the nozzle shear layer remain undisturbed over a distance which decreases with increasing Reynolds number.

Schlieren images are shown for hydrogen-flames at different conditions (Fig. 1). At the onset of disturbances the outer boundary suddenly widens up with the spreading angle increasing with increasing Reynolds number. The schlieren images also reveal longitudinal streaks occuring with the sudden expansion which are similar to streamwise streaks observed in a plane shear layer (Bernal and Roshko 1986).

Cross-sectional flow visualization by a light sheet reveals a star-like pattern with predominantly six spokes. This is shown, again for a hydrogen flame, in Fig. 2 at a height of four nozzle diameters above the burner exit.

Methane flames, as opposed to hydrogen flames, are attached to the burner only at moderate flow rates. However, up to that burner exit velocity u_0, at which a methane flame lifts off, it exhibits an azimuthal flow structure similar to that in hydrogen flames. Upstream from the base of a lifted methane flame, i.e. in the nonreacted methane jet, again a star-like flow pattern is observed as seen in Fig. 3. This cross-sectional view reveals more details of the inner structure in the cold jet than can be seen in the flame from Fig. 2. This might partly depend on too rapid vaporization of the light scattering water droplets in the outer flame zone.

In a study related to the present one on jet flames, a similar, very well organized star-like structure and the formation of radial jets were found in hot jets spreading in cold air (Monkewitz et al. 1988; Lehmann and Barsikow 1988).

In those jets, very strong self-sustained periodical ring vortices are produced due to absolute instability of the shear layer, if the ratio of the density of the jet, to the density of the surrounding fluid is below a critical value of 0.72 (Huerre and Monkewitz 1985; Monkewitz and Sohn 1986). Monkewitz et al. (1988) argue that the occurrence of a strongly organized star-like flow pattern and the formation of radial jets in the hot jet is due to azimuthal instability of the self-substained periodical ring vortices.

Azimuthal instability also occurs in single impulsively formed vortex rings, which was analysed by Widnall and Sullivan (1973) on the basis of a linear theory. And a similar star-like flow pattern was observed also in a cold air jet by Yule (1978), who related this to a deformation of toroidal vortices, resulting from Kelvin-Helmholtz-instability of the nozzle shear layer. A sketch explaining qualitatively the discussed flow pattern in flames is shown in Fig. 4.